1 Carbon Recycling Efficiency in Subduction Zones Constrained by the Effects of H₂O-CO₂ 2 Fluids on Partial Melt Compositions in the Mantle Wedge 3 4 Michael Lara* 5 6 Rajdeep Dasgupta 7 8 Department of Earth, Environmental and Planetary Sciences, Rice University, 6100 Main Street, 9 MS 126, Houston, TX 77005 10 11 12 **Abstract** 13 14 The extent of CO₂ transfer from subducting lithologies to the overlying mantle wedge in general 15 and to the arc magma source regions in particular remains debated. The limit of CO₂ transfer to 16 the sub-arc mantle could be estimated if the effects of CO₂ on the primary hydrous melt 17 compositions of mantle wedge can be assessed in relation to the observed compositions of 18 primitive arc magmas. Here we present new piston cylinder and multi-anvil experiments using 19 Au₇₅Pd₂₅ and Au capsules on four depleted peridotite $+ H_2O \pm CO_2$ starting compositions with 20 3.5 wt.% H_2O and XCO_2 [= molar CO_2 / ($CO_2 + H_2O$)] of 0-0.17. Experiments were performed at 21 2-4 GPa and 1200 °C to constrain how the presence of variable CO₂ in slab-derived aqueous 22 fluids affects the composition of peridotite partial melts. All experiments consisted of low degree 23 melts (<10 wt.%) in equilibrium with olivine + orthopyroxene ± clinopyroxene. Melts at 2-4 GPa 24 are basaltic for XCO₂ of 0-0.10 and become SiO₂-poor and CaO-rich at XCO₂ >0.10. 25 Comparison between our experimental partial melt compositions with a global dataset of the 26 most primitive arc magmas suggest that the upper limit of XCO₂ in fluids inducing melting in 27 mantle wedges is ~ 0.10 at 2-4 GPa. We apply these new constrains to an H₂O and CO₂ mass 28 balance model for subduction zones and estimate that at least 34-86% of CO₂ entering 29 subduction zones bypasses the sub-arc melt generation zone and is subducted to the convecting

mantle, either carried by the slab or by the down-dragged limb of the mantle wedge directly above the slab.

32

30

31

33

34

1. Introduction

35

36

37

38

39

40

41

42

43

44

45

46

47

48

49

50

51

52

The exchange of CO₂ and H₂O between Earth's surface and mantle reservoirs is driven by two key geological phenomena, namely subduction of oceanic lithosphere and volcanism. The relative flux of each mechanism sets the surface inventory of these life-essential volatiles and governs the long-term habitability of earth's surface. It is argued that the majority of CO₂ entering subduction zones does not resurface through arc volcanism but is rather carried within slabs to the deep mantle (Fig. 1A). This argument arises from (1) calculated imbalances between the flux of C in and out of subduction zones (Dasgupta and Hirschmann 2010; Johnston et al., 2011) (2) experiments and thermodynamic models demonstrating carbonate mineral stability in subducted lithologies through sub arc depths (Kerrick and Connolly 1998; Molina and Poli, 2000; Kerrick and Connolly 2001; Galvez et al., 2016). Such an imbalance, if not offset by midocean ridge/hotspot volcanism or metamorphic decarbonation, has the potential to transport all of earth's surface CO₂ to the mantle on the order of billions of years (Sleep and Zahnle, 2001). More recently, several authors have demonstrated that H₂O-rich fluid, derived from the breakdown of chlorite or serpentine in the subducting lithospheric mantle, may induce decarbonation and/or melting reactions in the overlying crust, thereby generating H₂O-CO₂ fluids at sub-arc depths (Connolly 2005; Gorman et al., 2006; Grassi and Schmidt 2011; Ague and

Nicolescu 2014; Kelemen and Manning 2015; Martin and Hermann 2018). Such a process may

significantly increase the recycling efficiency of CO_2 from the slab to the mantle wedge in subduction zones; however, the extent to which CO_2 is subducted past the mantle wedge melting zone (MWMZ) and into the deep mantle is still debated (Kelemen and Manning 2015; Plank and Manning 2019). More specifically, the CO_2 concentration of slab-derived fluids, hereafter written in terms of XCO_2 [= molar CO_2 / (CO_2 + H_2O)], remains uncertain yet is integral to evaluating the recycling efficiency of CO_2 and H_2O in subduction zones (Fig. 1A). This uncertainty, in large part, stems from the pathways the aqueous fluid takes and whether the fluids effectively interact with carbonate veins that may be unevenly distributed in the overlying crustal assemblages.

Many observations within natural arc systems suggest that CO₂ is at least a minor component in hydrous fluids fluxing the MWMZ. Melt inclusions hosted in arc lava phenocrysts contain up to 6 wt.% H₂O and 2500 ppm CO₂; however, considering the low solubility of CO₂ in silicate melts at crustal pressures, the CO₂ concentration of primary arc magmas are estimated to be > 3000 ppm (Wallace 2005) and as high as 1.5 wt. % (Blundy et al., 2010). C isotopes suggest that roughly two-thirds of carbon outflux in volcanic arcs is derived from subducted carbonates, suggesting that slab-derived CO₂ is a major source of carbon in the volcanic arc system (Shaw et al., 2003; de Leeuw et al., 2007). Finally, sub-arc mantle xenoliths discovered in multiple volcanic arcs around the world contain carbonate and hydrous minerals such dolomite, calcite, amphibole, and phlogopite, providing evidence for the ubiquity of H₂O-CO₂ fluid fluxing in mantle wedges globally (Ionov and Hofman 1995; McInnes et al., 2001; Laurora et al., 2001; Ducea et al., 2005; Sapienza et al., 2009).

Although H₂O and CO₂ are both recognized as important components in the mantle wedge fluids, very few experimental studies have explored the effects of H₂O-CO₂ fluids on

peridotite partial melt compositions. Previous studies concerned with the role of H₂O-CO₂ fluids on mantle melting were either conducted using simplified peridotite compositions (Eggler 1978; Wyllie 1978), focus primarily on solidus location, and do not report partial melt compositions (Olafsson and Eggler 1983), or are conducted over P-T conditions relevant for kimberlite/carbonatite genesis in the continental mantle lithosphere, i.e., at deeper conditions (Thibault et al., 1992; Wallace and Green 1998; Foley et al., 2009; Dvir and Kessel 2017; Fig. 1B). Furthermore, most of these studies were performed using CO₂ dominated starting compositions (Fig. 1B), whereas fluids inducing partial melting in the mantle wedge are likely dominated by H₂O (Molina and Poli 2000). As such, most previous studies exploring fluidinduced melting in the mantle wedge focus on the effects of H₂O alone and demonstrate that at 2-3 GPa, partial melts in peridotite + H₂O systems become increasingly SiO₂-rich and CaO-poor as the solidus is approached (Fig. 2). Conversely, partial melts from peridotite + CO₂ systems at 3 GPa become increasingly SiO₂-poor and CaO-rich as the solidus is approached (Dasgupta et al., 2007; Fig. 2). Therefore, the addition of CO₂ to slab-derived aqueous fluids could have a profound effect on peridotite partial melt composition relative to CO₂-free systems. However, to date, a systematic evaluation of how peridotite partial melt compositions change as a function of XCO₂ at mantle wedge *P-T* conditions is lacking. Here, we present melting phase relations and partial melt compositions from four peridotite + $H_2O \pm CO_2$ starting compositions with XCO₂ from 0 to 0.17 to explore how the gradual addition of CO₂ in slab-derived fluids affects the composition of peridotite partial melts. Experiments were run at 2-4 GPa and 1200 °C to simulate conditions of partial melt generation

in mantle wedges (Fig. 1). By comparing our partial melt compositions with primitive arc melts,

76

77

78

79

80

81

82

83

84

85

86

87

88

89

90

91

92

93

94

95

96

97

we constrain the XCO₂ of fluids inducing melting in the mantle wedge and further use this constraint in a new subduction zone H₂O and CO₂ mass balance model.

100

101

102

103

104

105

106

107

108

109

110

111

112

113

114

115

116

117

118

119

120

98

99

2. Methods

2.1 Starting Materials

Due to the depleted nature of many arc mantle xenoliths (Arai and Ishimaru 2007), the base peridotite composition used in this study is modeled after an unmetasomatised depleted peridotite xenolith (AVX-51) from the Kamchatka arc (Rapp et al., 1999; Kepezhinskas et al., 1995). Starting compositions were prepared to simulate partial melting of AVX-51 in the presence of H₂O-CO₂ fluids. The bulk H₂O content was held constant at 3.5 wt.% in all four starting compositions to isolate how the addition of small amounts of CO₂ in an otherwise identical fluid/rock system affects peridotite melting systematics. The bulk CO₂ contents of the four starting compositions are 0.00, 0.35, 1.05, 1.75 wt.%, corresponding to fluids with XCO₂ = 0.00, 0.04, 0.11, 0.17, respectively. The bulk compositions of the starting mixes (DP0, DP.04, DP.11, DP.17) are listed in Supplementary Table 1. The starting materials were synthesized using reagent grade oxides (SiO₂, Fe₂O₃, MnO, MgO), carbonates (CaCO₃, Na₂CO₃, K₂CO₃), hydroxides (Al(OH)₃, Mg(OH)₂), and hydrated magnesium carbonate (Mg₂(CO₃)(OH)₂.3H₂O). To minimize water adsorption, SiO₂, TiO₂, and MgO were heated overnight at 1000 °C, Fe₂O₃, CaCO₃, Na₂CO₃, and K₂CO₃ at 800 °C, and MnO at 300 °C. For the CO₂-free starting mix (DP0), SiO₂, Fe₂O₃, MnO, MgO, CaO, Na₂CO₃, and K₂CO₃ were mixed in the proportions of the calculated starting compositions and ground under ethanol for 1 h in an agate mortar. After the ethanol evaporated, the mixture was fired in a Deltech CO-CO2 gas mixing furnace at $\log fO_2 \sim FMQ - 2$ for 24 h to decarbonate the carbonate powders and reduce

Fe³⁺ to Fe²⁺. After reduction in the gas mixing furnace, Al(OH)₃ and Mg(OH)₂ were added in the proportion required to yield the desired bulk H₂O, MgO, and Al₂O₃ contents. The reduced powder plus the hydroxides were then ground under ethanol in an agate mortar for 1 h. The powder was collected in glass vial and stored at 110 °C in a drying oven. The previous steps were repeated for starting compositions DP.04 and DP.11, however CaCO₃ was added along with the hydroxides to yield the desired CaO and CO₂ concentrations. For DP.17, CO₂ was added as CaCO₃, Na₂CO₃, K₂CO₃, and hydrated magnesium carbonate (Mg₂(CO₃)(OH)₂.3H₂O). Hydrated magnesium carbonate was used due to the CO₂ content of the calculated starting composition exceeded that which can be held by CaCO₃, Na₂CO₃, and K₂CO₃ in the proportions necessary to meet the CaO, Na₂O, and K₂O requirements of the base depleted peridotite.

2.2. Experimental procedure

Experiments at 2-3 GPa were performed using a half-inch piston cylinder (PC) apparatus while experiments at 4 GPa were done using an 1100 ton Walker-style multi-anvil (MA) apparatus, both housed in the Experimental Petrology Laboratory at Rice University. All experiments were performed at 1200 °C to isolate the effects of XCO₂ and pressure on melt composition. The PC experiments were performed using a half-inch BaCO₃/MgO pressure media following the calibration and procedure of previous studies (Tsuno and Dasgupta 2011; Lara and Dasgupta 2020). The MA experiments were done using 18 mm MgO-Al₂O₃-SiO₂ Walker-style castable assembly following the calibration and procedure of Ding et al. (2014) and further described in Tsuno and Dasgupta (2015). The starting mixes were packed into 3 mm outer diameter Au₇₅Pd₂₅ capsules for PC experiments and into 2 mm outer diameter Au capsules for the MA experiments. The temperature for both PC and MA experiments was monitored using a

Type C thermocouple, accurate within ± 10 °C accounting for the thermal gradient across the assembly.

Experiments for each of the four starting compositions were run at 2, 3, and 4 GPa for durations of 97 – 143 h. The experiments were terminated by cutting off power to the heater and the assemblies were decompressed slowly. Once a capsule was retrieved from the PC or MA, it was mounted in Petropoxy 154 and stored in a furnace at 100 °C for 1 h to harden. The mounted capsule was ground on a 600 grit SiC paper to expose the material in the capsule. Once the material was exposed, the samples was impregnated with a low viscosity Petropoxy under vacuum to prevent pluck outs and loss of material from the capsule upon further polishing. The impregnated sample was then polished on a nylon cloth with 3 and 1 micron diamond powder.

2.3 Analysis of experimental products

Polished samples were first carbon-coated and then imaged and analyzed using a field emission gun electron microprobe (JEOL JXA-8530F Hyperprobe) at the Department of Earth, Environmental and Planetary Sciences at Rice University. Phases were identified using energy dispersive X-ray spectroscopy (EDS) and analyzed for major elements using wavelength dispersive X-ray spectroscopy (WDS) at an accelerating voltage of 15 kV. Minerals were analyzed using fully focused, 20 nA electron beam. If compositional zoning in a mineral was detected, analyses were taken along the rim as those analytical volumes are closer to equilibrium with adjacent phases. Melts were analyzed using a 10 nA defocused electron beam. Multiple spot analyses with beam sizes of 10-50 μm were performed evenly across each melt pool to ensure that the average composition was not biased by quench heterogeneity. Additionally, multiple

surfaces were polished across many experiments to check the homogeneity of silicate melts throughout the experimental capsule and to more reliably estimate the average composition of partial melt for each experiment (Supplementary Table 6).

170

171

172

173

174

175

176

177

178

179

180

181

182

183

184

185

186

187

188

189

167

168

169

3. Results

3.1 Textures, phase relations, and fluid saturation

Phase assemblages and proportions are listed in Supplementary Table 2 and backscattered electron images of experimental products are shown in Fig. 3. All experiments in this study contain an assemblage of melt + olivine + orthopyroxene \pm clinopyroxene. Olivines are euhedral with diameters >100 µm and are typically adjacent to melt pools (Fig. 3). Orthopyroxenes are euhedral but with much smaller diameters (<50 µm) while clinopyroxenes are present as both euhedral grains with diameters >100 μm often along capsule walls and as much smaller subhedral grains, which form networks along opx grain boundaries (Figs 3A and 3C). Pyroxenes are typically located on the opposite end the of capsule with respect the melt and olivine. Similar mineralogical gradients are observed in several hydrous peridotite studies and are attributed to thermal compaction effects (e.g., Lesher and Walker, 1998; Grove et al., 2006). Volatile-rich melts upon quenching and depressurization do not form homogeneous glasses but rather form an aggregate of volatile-rich metastable quench phases (Green 1973, 1976). Therefore, melt pool surfaces are rough and appear as aggregates of multiple phases with differing grayscales in back-scattered electron images (Figs 3B and 3D). Small quenched spherules observed along the capsule wall of experiment B491 (Supplementary Figure 4) is interpreted as a separate quenched aqueous fluid phase as demonstrated in past studies (Grove and Till 2019; Lara and Dasgupta 2020). Although this texture was only directly observed in one experiment, high total volatile contents of our starting mixes (3.50-5.25 wt.%) relative to the low degree melts produced (<10 wt.%) suggest that all our melts are fluid saturated. Indeed, if we assume that all H₂O and CO₂ enter the melt, mass balance calculations show that all melts have total volatile contents > 49 wt.%, much higher than our measured differences from 100% electron microprobe totals (Table 1). Therefore, we infer that all melts in this study are fluid saturated. Additionally, mass balance calculations show 25-30% Na₂O loss in our experiments relative to our bulk composition, likely reflecting Na₂O leaching into an H₂O-rich free fluid phase.

3.2. Mineral and melt compositions

All mineral compositions are listed in Supplementary Tables 3-5. Olivines are Fo₉₂₋₉₃, excluding olivines from experiments which suffered severe Fe loss. Orthopyroxenes are enstatite-rich (Mg# = 91.5-94.5; CaO = 0.5 - 1.3 wt.%; Al₂O₃ = 0.2 - 0.8 wt.%). Clinopyroxenes are Mg-rich augite (Mg# = 91.5-94.5; CaO = 18 - 21 wt.%; Al₂O₃ = 0.7 - 2.3 wt.%; Na₂O = 0.5 - 1.2 wt.%). No significant correlations between mineral composition, XCO₂, and pressure are observed in this study.

Initial mass balance calculations reveal that >15% Fe loss to metal capsules occurred in several experiments. Therefore, phase proportions are estimated by mass balance calculations excluding FeO* (Supplementary Table 2). Fe was added back to melts from experiments B498, B499, B495, MA271, MA269 and MA270 using methods described in Mallik et al. (2015). Fecorrected melt compositions are listed in Table 1 and plotted as a function of XCO₂ in Fig. 4. SiO₂, CaO, and Al₂O₃ all show systematic correlations with XCO₂ at a constant temperature (1200 °C). At 2 GPa, from bulk XCO₂ of 0 to 0.17, melt SiO₂ decreases from ~ 50 to 26 wt.%,

CaO increases from \sim 11 to 40 wt.%, and Al₂O₃ decreases from \sim 8 to 4 wt.%, with exception to the experiment at XCO₂ of 0.1 (Al₂O₃ = 12.5 wt.%). At 3-4 GPa, from XCO₂ of 0 to 0.17, melt SiO₂ decreases from \sim 46 to 36 wt.%, Al₂O₃ from \sim 14 to 6 wt.%, and CaO increases from \sim 10 to 25 wt.%. FeO*, MgO, Na₂O, and K₂O do not show obvious correlations with XCO₂ or pressure (Fig. 4). FeO* in our experiments ranges from \sim 10 to 6 wt.%, MgO \sim 22-12 wt.%, Na₂O \sim 4-2 wt.% and K₂O \sim 2.5-0.3 wt.%.

3.3. Approach to Equilibrium

The following criteria are used to establish maintenance of a closed system and a close approach to equilibrium. (a) Long experimental duration of 97-143 h, which exceed previous peridotite + H₂O \pm CO₂ melting studies demonstrating equilibrium at similar P-T conditions (e.g., Dvir and Kessel, 2017). (b) Small compositional heterogeneity within minerals as evident from replicate WDS analyses (Supplementary Tables 3-5). (c) Low sum of squared residuals in all experiments as demonstrated in mass balance calculations on an FeO*-free basis (Supplementary Table 2). (d) $K_{\rm DMelt}^{\rm Ol} = 0.24 - 0.43$ for all experiments, in agreement with this exchange coefficient (Roeder and Emslie 1970; Toplis 2005; Filiberto and Dasgupta, 2011).

4. Discussion

4.1 Comparison with previous peridotite $+ H_2O + CO_2$ studies

4.1.1. Effect of H₂O-CO₂ fluids on peridotite partial melt composition

Many previous studies demonstrated that both H₂O and CO₂ significantly alter the composition of mantle-derived melts (Kushiro, 1972; Green 1976; Hirose 1997; Gaetani and

Grove 1988; Grove et al., 2006; Dasgupta et al., 2007; Mitchell and Grove 2015; Grove and Till 2019; Sun and Dasgupta, 2019; Lara and Dasgupta 2020). Because melt compositions in peridotite + H₂O vs. peridotite + CO₂ systems diverge as the solidus is approached (Fig. 2), predicting melt compositions in peridotite + H₂O + CO₂ systems, particularly as a function of XCO₂, is not trivial. In Fig. 5, our melt compositions are plotted as a function of bulk XCO₂ and melt fraction and compared to melts from previous peridotite + H₂O + CO₂ studies on a volatile free basis (Wallace and Green 1988; Thibault et al., 1992; Foley et al., 2009; Brey et al., 2009; Dvir and Kessel 2017). These experimental data cover a range of bulk XCO₂, pressure, and temperature of 0.00-0.78, 2-6 GPa, and 900-1300 °C, respectively. From this comparison, it is evident that the composition of low degree melts (melt fraction <0.15) become CaO-MgO rich and SiO₂-Al₂O₃ poor as bulk XCO₂ increases, while at a given XCO₂, melts become increasingly CaO poor and SiO₂-Al₂O₃ rich as melt fraction increases (Fig. 5).

The trends observed in Fig. 5 are best explained by the documented effects of CO₂ on peridotite partial melt composition and are in contrast to trends observed in nominally CO₂-free, hydrous systems where low degree melts are typically enriched in SiO₂ and Al₂O₃ and depleted in MgO and CaO (Kushiro, 1972; Green 1976; Gaetani and Grove 1988; Grove et al., 2006; Mitchell and Grove 2015; Grove and Till 2019; Lara and Dasgupta 2020). The positive correlation between CO₂ and CaO in partial melts from CMAS + CO₂ and natural peridotite + CO₂ systems is well documented (e.g., Eggler, 1978; Hirose, 1997, Dasgupta et al., 2007; Sun and Dasgupta, 2019), resulting from reactions between Ca²⁺ cations and NBO-carbonate (CO₃²⁻) forming CaCO₃ complexes in silicate melts (Brooker et al., 2001). Similar reactions might also occur with Mg²⁺ cations (Duncan et al., 2017), which is supported by positive correlations between MgO and XCO₂ in H₂O-CO₂ bearing melts (Fig. 5), and in the nominally H₂O-free, CO₂

bearing melts from Dasgupta et al. (2007) and Mallik and Dasgupta (2014). Additionally, strong negative correlations are observed between CO₂ and SiO₂ in partial melts from CMAS + CO₂ and peridotite + CO₂ systems (Eggler 1978; Hirose 1997; Gudfinnsson and Presnall 2005; Dasgupta et al., 2007). This trend is explained by dilution of the melt with respect to SiO₂ by increases in dissolved CO₃²⁻ and associated 2+ cations (Ca²⁺, Mg²⁺) (Dasgupta et al., 2007). The negative correlation between CO₂ and Al₂O₃ in Fig. 5 is less understood; however, it is likely related to similar dilution effects. Considering that the compositional effects of CO₂ are more prominent in Fig. 5, even in H₂O-dominanted systems (XCO₂ <0.50), it appears that CO₂ poses a larger influence, relative to H₂O, on melt compositions in peridotite + H₂O + CO₂ systems at pressures \geq 2 GPa.

Owing to the highly incompatible nature of volatiles during partial melting, as melt fraction increases, the total volatile ($H_2O + CO_2$) concentrations in the melt decrease and thus are less affected by the compositional effects of H_2O and CO_2 . It is therefore not surprising that high degree melts are roughly basaltic in composition across the XCO_2 interval. This is also observed in peridotite + CO_2 and peridotite + H_2O systems, where partial melts converge to basaltic compositions (~ 42 wt.% SiO_2 ; ~ 10 wt.% CaO) as melting degree increases (Fig. 2).

4.1.2 Effects of total volatile content on melting in peridotite $+ H_2O + CO_2$ systems

Several peridotite + H_2O melting studies have demonstrated that starting compositions with higher bulk H_2O yield higher melt fractions at a given P and T (Mitchel and Grove 2015; Mallik et al., 2016; Lara and Dasgupta 2020). Whether the same correlation holds in in peridotite + H_2O + CO_2 systems is unknown. The starting compositions from Dvir and Kessel (2017) have identical XCO_2 (0.04 and 0.17) as two of our starting compositions, but with total volatile

contents $(H_2O + CO_2) \sim 3$ times greater than ours (Supplementary Table 1). Thus, this study offers an excellent comparison to evaluate how partial melting behavior changes as a function of total volatile content at a constant XCO_2 .

Considerably higher melt fractions (0.2-0.3) are reported in Dvir and Kessel (2017) relative to our experiments (Fig. 6). Considering that their experiments were run 100-300 °C lower yet still yield higher melt fractions, it is apparent that total volatile content greatly influences melt fraction in peridotite + H₂O + CO₂ systems. However, lower melt productivity is also expected in our depleted peridotite composition relative to the more fertile composition in Dvir and Kessel (2017) and therefore differences in melt fraction between these studies cannot be solely attributed to total volatile content. One interesting observation is that, despite the large difference in melt fraction between these two studies, SiO2 and CaO concentrations in the melts are similar for bulk compositions with equal XCO₂ (Fig. 6). This is likely due to a tradeoff between larger quantities of CO₂ available to dissolve in silicate melts and larger melt fractions, which both result from higher bulk volatile contents. In other words, it is conceivable that some low degree melts in this study have similar CO₂ concentrations as high degree melts from Dvir and Kessel (2017), thus explaining the similarities in CaO and SiO₂ melt composition. The difference in melt fraction does appear to have a larger effect on the concentrations of Na₂O and K₂O (Fig. 6). This is not surprising considering both the highly incompatible nature of alkalis during partial melting and the lesser effects of NBO-carbonate (CO₃²⁻) on +1 cations in silicate melts (Brooker et al., 2001). Whether the same trends and tradeoffs discussed above hold in CO₂ dominated systems is unknown and requires future experimental study.

303

304

282

283

284

285

286

287

288

289

290

291

292

293

294

295

296

297

298

299

300

301

302

4.2 Comparison with primitive arc melts and limits on CO₂ content in the sub-arc source regions

305

306

307

308

In this section, we compare our experimental melt compositions with natural primitive arc melts to constrain the fluid compositions that flux the sub-arc mantle wedge melting zone (MWMZ).

309

310

311

312

313

314

315

316

317

318

319

320

321

322

323

324

325

4.2.1 Primitive arc melts and fractionation corrections

Most arc melts sampled at the surface have undergone significant extents of fractional crystallization and or crustal assimilation since last equilibration with the mantle. Therefore, comparing experimental melts in equilibrium with mantle minerals with natural arc melts must first account for the complex fractionation and assimilation histories of arc melts. To overcome this complexity, we use the global primitive arc rock dataset compiled in Schmidt and Jagoutz (2017), which applies strict selection criteria (Equilibrium olivine Mg# = 0.87-0.91, Ni = 2000-4000 ppm) on >14000 volcanic arc whole rock data to select only arc lavas and dikes, which have been minimally altered since last equilibration with the mantle. This gave 938 primitive arc melts in equilibrium with an average Mg# olivine = 0.88; much lower compared to the average olivine produced in this study (Mg# \sim 0.92, Supplementary Table 3). Thus, to aptly compare our experimental melts with primitive arc melts, we have subtracted olivine from our melts until equilibrium with Mg# olivine = 0.88 are reached (Supplementary Material). In Fig. 7, we plot the compositions of our fractionation corrected melts on a volatile free basis and compare them to primitive arc melts from Schmidt and Jagoutz (2017) as well as to anomalously CaO-rich, silica undersaturated primitive melt inclusions from Schiano et al. (2000).

326

327

4.2.2 Upper XCO2 limits of mantle wedge fluids at 1200 °C

In Fig. 7, bulk compositions with XCO₂ = 0.17 generate melts at 1200 °C with SiO₂, CaO, and Al₂O₃ compositions, which lie exceedingly far from all primitive arc melts. This suggests that $XCO_2 = 0.17$ far exceeds the upper limit of fluids in the MWMZ, in agreement with slab decarbonation models from Gorman et al. (2006) and Galvez et al. (2016). More specifically, the highest XCO₂ which can reproduce primitive arc melt compositions is 0.10 at 2-4 GPa, thereby setting limits on CO₂, relative to H₂O, present in the MWMZ. This is not an artifact of the fractionation corrections applied to our melts as the same conclusion holds when comparing our original uncorrected melt compositions to primitive arc melts (Supplementary Figure 2). The exception is that all our uncorrected melts have systematically higher MgO and lower Al₂O₃ concentrations with respect to primitive arc melts; likely a consequence of the latter having undergone olivine fractionation. Fractional crystallization experiments have also demonstrated that cpx in addition to olivine lies close the liquidus of hydrous arc melts at lower crustal pressures (Blatter et al., 2013; Nandedkar et al., 2014). Therefore, we applied a second fractionation correction to our melts where we subtract ½ mass unit of cpx for every 1 mass unit of olivine until melts are in equilibrium with olivine Mg# = 0.88 (Supplementary Materials). These corrected arc melts are compared to primitive arc melts in Supplementary Figure 3. Even when correcting for cpx and olivine fractionation, the conclusions drawn from Fig. 7 hold. It is reasonable then to conclude that fluids in the MWMZ are very CO₂ poor and specifically with upper XCO₂ limits at 1200 °C ~ 0.10 at 2-4 GPa. We note that this XCO₂ limit appears smaller at 2 GPa; however, due to large uncertainties in SiO₂, CaO and Al₂O₃ concentrations in the melt from the experiment (B498) at 2 GPa with $XCO_2 = 0.10$ (Figure. 4), we are cautious to set constraints at XCO₂ < 0.10.

328

329

330

331

332

333

334

335

336

337

338

339

340

341

342

343

344

345

346

347

348

349

351

352

353

354

355

356

357

358

359

360

361

362

363

364

365

366

367

368

369

370

371

372

373

Our experimental constraints on the effects of XCO₂ on peridotite partial melt compositions are at 1200 °C. However, many geodynamic models predict maximum mantle wedge temperatures beneath arcs upwards of 1400 °C (e.g., Syracuse et al., 2010, England and Katz, 2010; Fig. 1A). Therefore, it is possible that some arc melts are generated at higher temperatures than our experimental temperature of choice (1200 °C). To evaluate whether similar XCO₂ limits would hold at higher temperatures, we estimate melt fractions at 1400 °C for bulk compositions with $XCO_2 = 0.17$ at 2-4 GPa using isobaric melt productivities (IMP) of 5.8 and 7.9 wt.%/100 °C at 2 and 3-4 GPa, respectively, from Lara and Dasgupta (2020). These IMP's are used because they were derived using the same base peridotite composition with identical H₂O contents (3.5 wt.%) as this study and therefore we expect similar melt productivities in our experiments. We estimate that at 1400 °C, bulk compositions with XCO₂ = 0.17 at 2 GPa would generate 13.58 wt.% melt and bulk compositions with XCO₂ = 0.17 at 3-4 GPa would generate 20.1 wt.% melt. If we assume that all CO₂ in our bulk compositions is present in the melt, then at 1400 °C, melt CO₂ concentrations are estimated to be 11.04 wt.% for bulk compositions with XCO₂ = 0.17 at 2 GPa and 8.71 wt.% for bulk compositions with XCO₂ = 0.17 at 3-4 GPa. Using empirically derived equation of melt CO₂ vs. melt SiO₂ from Dasgupta et al. (2007) (See Supplementary Methods), we calculate SiO₂ concentrations of 36.4 wt.% for bulk compositions with XCO₂ = 0.17 at 2 GPa and 38.5 wt.% for bulk compositions with XCO₂ = 0.17 at 3-4 GPa. Given that the melt SiO₂ estimates at 1400 °C are still much less than even the most SiO₂-poor primitive arc melts and that 1400 °C is close to the thermal maximum in mantle wedges (England and Katz, 2010), we consider it likely that the XCO₂ limits derived from 1200 °C experiments will apply to all mantle wedge thermal conditions and thus would apply globally.

However, due to a lack of experimental partial melt compositional data in peridotite + H₂O + CO₂ systems at temperatures >1200 °C (Fig. 1B), the combined effects of H₂O and CO₂ on melt productivities at higher temperatures cannot be fully assessed and requires future experimental study.

378

379

374

375

376

377

- 4.3 Implications for the Deep Carbon Cycle
- 380 Given that our experimental partial melt compositions and their comparisons with primitive arc
- basalts constrain the relative abundance of H₂O and CO₂ in the MWMZ, we can use this
- information to constrain on the efficiency of carbon recycling in subduction zones.

383

384 *4.3.1 CO₂ and H₂O mass balance in subduction zones*

385

- In equations 1 and 2 below and as illustrated in Supplementary Fig. S3A, we describe a simple
- mass balance of CO₂ and H₂O in subduction zones.

$$CO_{2in} = CO_{2f} + CO_{2w} + CO_{2m}$$
 (1)

$$H_2 O_{in} = H_2 O_f + H_2 O_w + H_2 O_m \tag{2}$$

390

- Where CO_{2in} is the global flux of CO₂ entering subduction trenches in (g/y) and CO_{2f} , CO_{2w} ,
- and CO_{2m} are the global flux of CO₂ entering the forearc mantle, mantle wedge melting zone
- 393 (MWMZ), and deep mantle, respectively in g/y. Similar notation is used for H₂O mass balance
- 394 (equation 2). Dividing all terms by CO_{2in} or H_2O_{in} yields

395

$$1 = C_f + C_w + C_m (3)$$

$$1 = H_f + H_w + H_m \tag{4}$$

398

Where C_f , C_w and C_m are the flux of CO₂ entering the forearc mantle, MWMZ, and deep mantle

400 relative to CO_{2in} . Similar notation is used for H₂O (equation 4).

401

402 Considering,

$$C_w = \frac{co_{2w}}{co_{2in}} \tag{5}$$

$$404 H_w = \frac{H_2 O_w}{H_2 O_{in}} (6)$$

405 Then,

$$\frac{C_w}{H_w} = \frac{CO_{2w}}{CO_{2in}} \times \frac{H_2O_{in}}{H_2O_w} \tag{7}$$

407 Now considering,

$$408 e = \frac{CO_{2w}}{H_2O_w} (8)$$

409

Where e = 0.27 is our experimentally determined limit for wt.% CO₂ divided by wt.% H₂O

411 entering the MWMZ (equivalent to $XCO_2 = 0.1$). Combing equations 7 and 8 yields

412

$$C_w = \frac{H_2 O_{in}}{C O_{2in}} \times e \times H_w \tag{9}$$

414 For simplicity we denote,

$$\frac{H_2 O_{in}}{c O_{2in}} = H C_{in} \tag{10}$$

416

417 Plugging equations 9 and 10 back into equation 3 and rearranging yields,

 $C_m = 1 - C_f - HC_{in} \times e \times H_w \tag{11}$

Note that the fraction of subducted CO_2 that enters the deep mantle (C_m) depends only on 4 non-dimensional numbers; (1) fraction of subducted CO_2 entering the forearc mantle (C_f) (2) H_2O/CO_2 ratio of incoming oceanic lithosphere (crust + mantle) (HC_{in}) (3) our experimentally determined maximum CO_2/H_2O in the MWMZ (e); assumed to be supplied chiefly by slab devolatilization and (4) fraction of subducted H_2O entering the MWMZ (H_w) . The subduction zone mass balance in terms on non-dimensional numbers is further illustrated in Supplementary Fig. S3B. To determine input values or ranges for each non-dimensional term in equation 11, we compile H_2O and CO_2 flux estimates in subduction zones from existing literature in Table 2.

4.3.2 Estimating input parameters

Several studies have attempted to quantify the global flux of mineral bound CO₂ or H₂O entering subduction zones; however, most of these studies only provide estimates for CO₂ or H₂O independently. Therefore, internally consistent estimates for HC_{in} are mostly unavailable in the existing literature with the exception to Jarrard (2003) who estimate a value of 4.9 (Table 2). To select a reasonable range of HC_{in} , we ran 1000 Monte Carlo simulations using the ranges of H_2O_{in} and CO_{2in} listed in Table 2 and found an average $HC_{in} \sim 5 \pm 2$ (1 σ). This suggests that around five times more mineral bound H₂O enters subduction zones by weight globally relative to CO₂; however, it should be noted that the H₂O and CO₂ content of the oceanic lithospheric mantle remains highly uncertain (Hacker 2008; Kelemen and Manning 2015) and therefore the average and range of HC_{in} is subject to change.

Kelemen and Manning (2015) use thermodynamic modeling to estimate that the global CO₂ flux to the fore-arc mantle (> 2GPa) is about 0.3-3% of CO_{2in} , while more recently Barry et al. (2019) used helium and carbon isotope data from deeply sourced springs beneath the Costa Rican forearc to estimate that 0.1–12% of CO₂ entering the Costa Rican subduction zone is released through the fore-arc. Since both studies estimate $C_f \le 0.12$ using differing methods and applied to different spatial scales, we find it reasonable to consider a maximum C_f of 0.12.

Finally, several studies have estimated the flux of H_2O entering the mantle wedge relative to the flux of H_2O entering subduction trenches (Ito et al., 1981, Peacock 1990; Schmidt and Poli 1998, 2003; Van Keken et al., 2011). These studies predict that about 10-40% of subducted H_2O fluxes the mantle wedge, while the remaining 60 - 90% is either released to the fore-arc mantle or subducted beyond the arc to the deep mantle (Hacker 2008). Therefore, we vary H_w from 0.1 - 0.4 and further discriminate mantle wedge H_2O fluxes in cold ($H_w = 0.1$ -0.25) vs. hot ($H_w = 0.25$ -0.4) subduction zones according to Schmidt and Poli (1998).

4.3.3 Fraction of subducted CO2 entering the deep mantle

In Fig. 8A and 8B, we plot solutions to equation 11 on 2D contour maps covering the ranges of HC_{in} , C_f , and H_w determined in Table 2. To evaluate the likelihood of subducted CO_2 returning to the deep mantle, we calculate C_m values in Fig. 8 by evaluating equation 11 using our experimentally determined maximum value e = 0.27 at 2-4 GPa. If we assume that $HC_{in} = 5$ and the fraction of subducted CO_2 that enters forearc is negligible ($C_f = 0$) (Kerrick and Connolly., 2001; Kelemen and Manning., 2015), then we predict that 46-86 % of subducted CO_2 enters the deep mantle (Fig. 8A). If we assume $HC_{in} = 5$ and up to 12% of subducted CO_2 enters the forearc as suggested in the field based study of Barry et al. (2019), then we still predict that

34-74 % of subducted CO₂ will enter the deep mantle (Fig. 8B). The exception to these constraints occurs only if HC_{in} and H_w are near their estimated maximum values, for example if H_2O is ~ 7 times more abundant than CO_2 within an incoming slab entering a hot subduction zone (Figure 8B). In this scenario, the majority of subducted CO₂ may be released to the mantle wedge as CO₂-poor fluids, thereby meeting the constraints set by e. However, because most of the parameter space considered in Fig. 8 predicts a $C_m = 0.34 - 0.86$, we consider it likely that 34-86% of CO₂ entering subduction zones globally bypasses the MWMZ and is subducted to the deep mantle (Figure 8C). We note that while our approach predicts low XCO₂ fluids in the MWMZ, it does not rule out potentially high CO₂ fluxes from the subducting slab (crust + mantle lithosphere) to the sub-solidus mantle directly above the slab. Reaction between peridotite and H₂O-CO₂ fluids or H₂O-CO₂-bearing melts at sub-solidus conditions (<1000 °C) can precipitate hydrous and carbonate minerals (e.g., Saha et al., 2018, 2021; Saha and Dasgupta, 2019), thereby potentially inhibiting some slab-derived H₂O and CO₂ from fluxing the hotter core of mantle wedge and influencing arc magma generation. This sub-solidus mantle wedge region, however, would get dragged down with the slab (Fig. 1) and in either case, CO₂ does not get recycled into the MWMZ and enters the deep mantle.

480

481

482

483

484

485

486

464

465

466

467

468

469

470

471

472

473

474

475

476

477

478

479

5. Concluding remarks

In order to constrain the effect of dissolved CO₂ in slab-derived aqueous fluid on primary melt compositions generated in the mantle wedge, we ran high *P-T* experiments on depleted peridotite + H₂O + CO₂ at conditions relevant for slab-derived flux melting in the mantle wedge (2 - 4 GPa, 1200 °C). We systematically varied XCO₂ of starting compositions from 0.00 to 0.17. We find that as XCO₂ increases at a constant pressure and temperature, the CaO concentrations

487	of partial melts systematically increase while the SiO2 and Al2O3 contents systematically
488	decrease. Comparing our experimental melts to natural primitive arc melts, we find that fluids
489	with $XCO_2 \ge 0.10$, at 2-4 GPa produce melts which lie exceedingly far from all primitive arc
490	melts in terms of CaO, SiO ₂ , and Al ₂ O ₃ , thereby setting constraints on the XCO ₂ of fluids fluxing
491	mantle wedges beneath arcs. Applying these XCO2 constraints in an H2O-CO2 subduction mass
492	balance model, we demonstrate that among most conceivable subduction scenarios (incoming
493	plate compositions, thermal structure), 34-86 % of CO ₂ entering subduction zones globally is
494	likely transported to the deep mantle, either being hosted in subducting slab lithologies or as part
495	of the down-dragged limb of the mantle wedge.
496	
497	Acknowledgments

- We gratefully acknowledge supportive, yet critical reviews by Peter Ulmer and an anonymous
- 499 reviewer. This work received support from NSF grant EAR-1763226.

501 References

498

500

- 502 Ague, J.J., Nicolescu, S., 2014. Carbon dioxide released from subduction zones by fluid-503 mediated reactions. Nat. Geosci. 7, 355–360.
- 504 Arai, S., Ishimaru, S., 2007. Insights into Petrological Characteristics of the Lithosphere of 505 Mantle Wedge beneath Arcs through Peridotite Xenoliths: a Review. J. Petrol. 49, 665–695.
- 506 Barry, P.H., de Moor, J.M., Giovannelli, D., Schrenk, M., Hummer, D.R., Lopez, T., Pratt, C.A.,
- 507 Segura, Y.A., Battaglia, A., Beaudry, P., Bini, G., Cascante, M., d'Errico, G., di Carlo, M.,
- 508 Fattorini, D., Fullerton, K., Gazel, E., González, G., Halldórsson, S.A., Iacovino, K.,
- 509 Kulongoski, J.T., Manini, E., Martínez, M., Miller, H., Nakagawa, M., Ono, S., Patwardhan,
- 510 S., Ramírez, C.J., Regoli, F., Smedile, F., Turner, S., Vetriani, C., Yücel, M., Ballentine,
- 511 C.J., Fischer, T.P., Hilton, D.R., Lloyd, K.G., 2019. Forearc carbon sink reduces long-term
- volatile recycling into the mantle. Nature 568, 487–492. 512
- 513 Bebout, G.E., 1995. The impact of subduction-zone metamorphism on mantle-ocean chemical 514 cycling. Chem. Geol. 126, 191–218.

- 515 Blatter, D.L., Sisson, T.W., Hankins, B.W., 2013. Crystallization of oxidized, moderately
- 516 hydrous arc basalt at mid-to lower-crustal pressures: implications for andesite genesis.
- 517 Contrib Mineral Petrol 166, 861-886.
- 518 Blundy, J., Cashman, K. V., Rust, A., Witham, F., 2010. A case for CO₂-rich arc magmas. Earth
- 519 Planet. Sci. Lett. 290, 289–301.
- 520 Brey, G.P., Bulatov, V.K., Girnis, A. V., 2009. Influence of water and fluorine on melting of
- 521 carbonated peridotite at 6 and 10 GPa. Lithos 112, 249–259.
- Brooker, R.A., Kohn, S.C., Holloway, J.R., McMillan, P.F., 2001. Structural controls on the
- solubility of CO2 in silicate melts Part II: IR characteristic of carbonate groups in silicate
- 524 glasses. Chem. Geol. 174, 241–254.
- 525 Connolly, J.A.D., 2005. Computation of phase equilibria by linear programming: A tool for
- geodynamic modeling and its application to subduction zone decarbonation. Earth Planet.
- 527 Sci. Lett. 236, 524–541.
- 528 Dasgupta, R., 2013. Ingassing, Storage, and Outgassing of Terrestrial Carbon through Geologic
- Time. Rev. Mineral. Geochemistry 75, 183–229.
- Dasgupta, R., Hirschmann, M.M., 2010. The deep carbon cycle and melting in Earth's interior.
- 531 Earth Planet. Sci. Lett. 298, 1-13.
- Dasgupta, R., Hirschmann, M.M., Smith, N.D., 2007. Partial melting experiments of peridotite +
- 533 CO₂ at 3 GPa and genesis of alkalic ocean island basalts. J. Petrol. 48, 2093–2124.
- de Leeuw, G.A.M., Hilton, D.R., Fischer, T.P., Walker, J.A., 2007. The He-CO₂ isotope and
- relative abundance characteristics of geothermal fluids in El Salvador and Honduras: New
- 536 constraints on volatile mass balance of the Central American Volcanic Arc. Earth Planet.
- 537 Sci. Lett. 258, 132–146.
- 538 Ding, S., Dasgupta, R., Tsuno, K., 2014. Sulfur concentration of martian basalts at sulfide
- saturation at high pressures and temperatures Implications for deep sulfur cycle on Mars.
- 540 Geochim. Cosmochim. Acta 131, 227–246.
- Ducea, M.N., Saleeby, J., Morrison, J., Valencia, V.A., 2005. Subducted carbonates,
- metasomatism of mantle wedges, and possible connections to diamond formation: An
- example from California. Am. Mineral. 90, 864–870.
- Dvir, O., Kessel, R., 2017. The effect of CO₂ on the water-saturated solidus of K-poor peridotite
- between 4 and 6 GPa. Geochim. Cosmochim. Acta 206, 184–200.
- Eggler, D. H., 1978. The effect of CO₂ upon partial melting of peridotite in the system Na₂O-
- CaO-Al₂O₃-MgO-SiO₂-CO₂ to 35 kb, with an analysis of melting in a peridotite-H₂O-CO₂
- 548 system. Am. J. Sci. 278, 305-343

- England, P.C., Katz, R.F., 2010. Melting above the anhydrous solidus controls the location of volcanic arcs. Nature. 467, 700–703.
- Falloon, T.J., Green, D.H., 1990. Solidus of carbonated fertile peridotite under fluid-saturated conditions. Geology 18, 195–199.
- Filiberto, J., Dasgupta, R., 2011. Fe2+–Mg partitioning between olivine and basaltic melts:
- Applications to genesis of olivine-phyric shergottites and conditions of melting in the
- Martian interior. Earth Planet. Sci. Lett. 304, 527–537.
- Foley, S.F., Yaxley, G.M., Rosenthal, A., Buhre, S., Kiseeva, E.S., Rapp, R.P., Jacob, D.E.,
- 557 2009. The composition of near-solidus melts of peridotite in the presence of CO₂ and H₂O
- between 40 and 60 kbar. Lithos 112, 274–283.
- Galvez, M.E., Connolly, J.A.D., Manning, C.E., 2016. Implications for metal and volatile cycles from the pH of subduction zone fluids. Nature 539, 420–424.
- Gaetani, G.A., Grove, T.L., 1998. The influence of water on melting of mantle peridotite.
- 562 Contrib Mineral Petrol 131, 323-346.
- Gorman, P.J., Kerrick, D.M., Connolly, J.A.D., 2006. Modeling open system metamorphic
- decarbonation of subducting slabs. Geochemistry, Geophys. Geosystems 7.
- 565 https://doi.org/10.1029/2005GC001125
- Grassi, D., Schmidt, M.W., 2011. The melting of carbonated pelites from 70 to 700 km depth. J. Petrol. 52, 765–789.
- Green, D.H., 1976. Experimental testing of "equilibrium" partial melting of peridotite under water-saturated, high-pressure conditions. Canadian Mineralogist. 14, 255-268
- 570 Green, D.H., 1973. Experimental melting studies on a model upper mantle composition at high
- 571 pressure under water-saturated and water-undersaturated conditions. Earth Planet. Sci. Lett.
- 572 19, 37–53.
- Grove, T., Parman, S., Bowring, S., Price, R., Baker, M., 2002. The role of an H₂O-rich fluid
- component in the generation of primitive basaltic andesites and andesites from the Mt.
- 575 Shasta region, N California. Contrib. to Mineral. Petrol. 142, 375–396.
- 576 Grove, T.L., Chatterjee, N., Parman, S.W., Médard, E., 2006. The influence of H₂O on mantle wedge melting. Earth Planet. Sci. Lett. 249, 74–89.
- Grove, T.L., Till, C.B., 2019. H₂O-rich mantle melting near the slab-wedge interface. Contrib. to
- 579 Mineral. Petrol. 174, 80.

- Gudfinnsson, G.H., Presnall, D.C., 2005. Continuous Gradations among Primary Carbonatitic,
- Kimberlitic, Melilititic, Basaltic, Picritic, and Komatiitic Melts in Equilibrium with Garnet
- 582 Lherzolite at 3–8 GPa. J. Petrol. 46, 1645–1659.
- Hacker, B.R., 2008. H 2 O subduction beyond arcs. Geochemistry, Geophys. Geosystems 9.
- 584 https://doi.org/10.1029/2007GC001707
- 585 Hirose, K., 1997. Partial melt compositions of carbonated peridotite at 3 GPa and role of CO₂ in
- alkali-basalt magma generation. Geophys. Res. Lett. 24, 2837–2840.
- Ionov, D.A., Hofmann, A.W., 1995. NbTa-rich mantle amphiboles and micas: Implications for
- subduction-related metasomatic trace element fractionations. Earth Planet. Sci. Lett. 131,
- 589 341–356.
- 590 Ito, E., Harris, D.M., Anderson, A.T., 1983. Alteration of oceanic crust and geologic cycling of
- chlorine and water. Geochim. Cosmochim. Acta 47, 1613–1624.
- Jarrard, R.D., 2003. Subduction fluxes of water, carbon dioxide, chlorine, and potassium.
- Geochemistry, Geophys. Geosystems 4. https://doi.org/10.1029/2002GC000392
- Johnston, F.K.B., Turchyn, A. V., Edmonds, M., 2011. Decarbonation efficiency in subduction
- zones: Implications for warm Cretaceous climates. Earth Planet. Sci. Lett. 303, 143–152.
- Kelemen, P.B., Manning, C.E., 2015. Reevaluating carbon fluxes in subduction zones, what goes
- down, mostly comes up. PNAS 112, 2020.
- Kepezhinskas, P.K., Defant, M.J., Drummond, M.S., 1995. Na Metasomatism in the Island-Arc
- Mantle by Slab Melt—Peridotite Interaction: Evidence from Mantle Xenoliths in the North
- 600 Kamchatka Arc. J. Petrol. 36, 1505–1527.
- Kerrick, D.M., Connelly, J.A.D., 2001. Metamorphic devolatilization of subducted marine
- sediments and the transport of volatiles into the Earth's mantle. Nature 411, 293–296.
- Kerrick, D.M., Connolly, J.A.D., 1998. Subduction of ophicarbonates and recycling of CO₂ and
- 604 H2O. Geology 26, 375–378.
- Kushiro, I., 1972. Effect of Water on the Composition of Magmas Formed at High Pressures. J.
- 606 Petrol. 13, 311–334.
- Lara, M., Dasgupta, R., 2020. Partial melting of a depleted peridotite metasomatized by a
- MORB-derived hydrous silicate melt Implications for subduction zone magmatism.
- 609 Geochim. Cosmochim. Acta 290, 137–161.
- 610 Laurora, A., Mazzucchelli, M., Rivalenti, G., Vannucci, R., Zanetti, A., Barbieri, M.A.,
- Cingolani, C.A., 2001. Metasomatism and melting in carbonated peridotite xenoliths from

612 613	the mantle wedge: The Gobernador Gregores case (Southern Patagonia). J. Petrol. 42, 69–87.
614 615 616 617	Lee, CT.A., Luffi, P., Chin, E.J., 2011. Building and Destroying Continental Mantle. Annual Review of Earth and Planetary Sciences, vol. 39, Annual Reviews, Palo Alto (2011), pp. 59-90
618 619	Lesher, C.E., Walker, D., 1988. Cumulate Maturation and Melt Migration in a Temperature Gradient, J. Geophys. Res. 93 (B9) 10295-10311.
620 621 622 623	Mallik, A., Dasgupta, R., 2014. Effect of variable CO2 on eclogite-derived andesite and lherzolite reaction at 3 GPa—Implications for mantle source characteristics of alkalic ocean island basalts. Geochemistry, Geophys. Geosystems 15. https://doi.org/10.1002/2014GC005251
624 625 626 627	Mallik, A., Nelson, J., Dasgupta, R., 2015. Partial melting of fertile peridotite fluxed by hydrous rhyolitic melt at 2–3 GPa: implications for mantle wedge hybridization by sediment melt and generation of ultrapotassic magmas in convergent margins. Contrib. to Mineral. Petrol. 169, 48.
628 629 630	Mallik, A., Dasgupta, R., Tsuno, K., Nelson, J., 2016. Effects of water, depth and temperature on partial melting of mantle-wedge fluxed by hydrous sediment-melt in subduction zones. Geochim. Cosmochim. Acta 195, 226–243.
631 632	Martin, L.A.J., Hermann, J., 2018. Experimental phase relations in altered oceanic crust: Implications for carbon recycling at subduction zones. J. Petrol. 59, 299–320.
633 634 635 636	McInnes, B.I.A., Gregoire, M., Binns, R.A., Herzig, P.M., Hannington, M.D., 2001. Hydrous metasomatism of oceanic sub-arc mantle, Lihir, Papua New Guinea: Petrology and geochemistry of fluid-metasomatised mantle wedge xenoliths. Earth Planet. Sci. Lett. 188, 169–183.
637 638	Mitchell, A.L., Grove, T.L., 2015. Melting the hydrous, subarc mantle: the origin of primitive andesites. Contrib. to Mineral. Petrol. 170, 13.
639 640	Molina, J.F., Poli, S., 2000. Carbonate stability and fluid composition in subducted oceanic crust: An experimental study on H2O-CO2-bearing basalts. Earth Planet. Sci. Lett. 176, 295–310.
641 642	Nandedkar, R.H., Ulmer, P., Müntener, O., 2014. Fractional crystallization of primitive, hydrous arc magmas: An experimental study at 0.7 GPa. Contrib. to Mineral. Petrol. 167, 1–27.
643 644 645	Olafsson, M., Eggler, D.H., 1983. Phase relations of amphibole, amphibole-carbonate, and phlogopite-carbonate peridotite: petrologic constraints on the asthenosphere. Earth Planet. Sci. Lett. 64, 305-315.

- Peacock, S.M., 1990. Fluid processes in subduction zones. Science. 248, 329–337.
- Pirard, C., Hermann, J., 2015. Focused fluid transfer through the mantle above subduction zones.
- Geology 43, 915–918.
- Plank, T., Manning, C.E., n.d. Subducting carbon. Nature. 574, 343-352
- Rapp, R.., Shimizu, N., Norman, M.., Applegate, G.., 1999. Reaction between slab-derived melts
- and peridotite in the mantle wedge: experimental constraints at 3.8 GPa. Chem. Geol. 160,
- Roeder, P.L., Emslie, R.F., 1970. Olivine-liquid equilibrium. Contrib. to Mineral. Petrol. 29,
- 653 275–289.
- Rüpke, L.H., Morgan, J.P., Hort, M., Connolly, J.A.D., 2004. Serpentine and the subduction
- zone water cycle. Earth Planet. Sci. Lett. 223, 17–34.
- Saha, S., Dasgupta, R., Tsuno, K., 2018. High Pressure Phase Relations of a Depleted Peridotite
- Fluxed by CO₂ -H₂ O-Bearing Siliceous Melts and the Origin of Mid-Lithospheric
- Discontinuity. Geochemistry, Geophys. Geosystems 19, 595–620.
- https://doi.org/10.1002/2017GC007233
- Saha, S., Dasgupta, R., 2019. Phase Relations of a Depleted Peridotite Fluxed by a CO2-H2O
- Fluid—Implications for the Stability of Partial Melts Versus Volatile-Bearing Mineral
- Phases in the Cratonic Mantle. J. Geophys. Res. Solid Earth 124, 10089–10106.
- Saha, S., Peng, Y., Dasgupta, R., Mookherjee, M., Fischer, K.M., 2021. Assessing the presence
- of volatile-bearing mineral phases in the cratonic mantle as a possible cause of mid-
- lithospheric discontinuities. Earth Planet. Sci. Lett. 553, 116602.
- Sapienza, G.T., Marco, A.E., Ae, S., Braga, R., Scambelluri, M., 2009. Dolomite-bearing
- orogenic garnet peridotites witness fluid-mediated carbon recycling in a mantle wedge
- 668 (Ulten Zone, Eastern Alps, Italy). Contrib Miner. Pet. 158, 401–420.
- 669 Schiano, P., Eiler, J.M., Hutcheon, I.D., Stolper, E.M., 2000. Primitive CaO-rich, silica-
- undersaturated melts in island arcs: Evidence for the involvement of clinopyroxene-rich
- lithologies in the petrogenesis of arc magmas. Geochemistry, Geophys. Geosystems 1.
- https://doi.org/10.1029/1999GC000032
- 673 Schmidt, M.W., Jagoutz, O., 2017. The global systematics of primitive arc melts. Geochemistry,
- Geophys. Geosystems 18, 2817–2854. https://doi.org/10.1002/2016GC006699
- 675 Schmidt, M.W., Poli, S., 2003. Generation of Mobile Components during Subduction of Oceanic
- 676 Crust. Treatise on Geochemistry., 3-9, 567–591.
- 677 Schmidt, M.W., Poli, S., 1998. Experimentally based water budgets for dehydrating slabs and
- consequences for arc magma generation. Earth Planet. Sci. Lett. 163, 361–379.

- 679 Shaw, A.M., Hilton, D.R., Fischer, T.P., Walker, J.A., Alvarado, G.E., 2003. Contrasting He-C
- relationships in Nicaragua and Costa Rica: Insights into C cycling through subduction
- 681 zones. Earth Planet. Sci. Lett. 214, 499–513.
- 682 Sisson, T.W., Grove, T.L., 1993. Temperatures and H₂O contents of low-MgO high-alumina
- basalts. Contrib. to Mineral. Petrol. 113, 167–184.
- Sleep, N.H., Zahnle, K., 2001. Carbon dioxide cycling and implications for climate on ancient
- Earth. J. Geophys. Res. E Planets 106, 1373–1399.
- Sun, C., Dasgupta, R., 2019. Slab–mantle interaction, carbon transport, and kimberlite generation
- in the deep upper mantle. Earth Planet. Sci. Lett. 506, 38–52.
- 688 Syracuse, E.M., van Keken, P.E., Abers, G.A., 2010. The global range of subduction zone
- thermal models. Phys. Earth Planet. Inter. 183, 73–90.
- Toplis, M.J., 2005. The thermodynamics of iron and magnesium partitioning between olivine
- and liquid: Criteria for assessing and predicting equilibrium in natural and experimental
- 692 systems. Contrib. to Mineral. Petrol. 149, 22–39.
- Thibault, Y., Edgar, A.D., Loyd, F.E., 1992. Experimental investigation of melts from a
- carbonated phlogopite lherzolite: Implications for metasomatism in the continental
- 695 lithospheric mantle, American Mineralogist. 77 (7-8), 784-794
- Tsuno, K., Dasgupta, R., 2011. Melting phase relation of nominally anhydrous, carbonated
- 697 pelitic-eclogite at 2.5–3.0 GPa and deep cycling of sedimentary carbon. Contrib. to Mineral.
- 698 Petrol. 161, 743–763.
- Tsuno, K., Dasgupta, R., 2015. Fe-Ni-Cu-C-S phase relations at high pressures and temperatures
- The role of sulfur in carbon storage and diamond stability at mid- to deep-upper mantle.
- 701 Earth Planet. Sci. Lett. 412, 132–142.
- van Keken, P.E., Hacker, B.R., Syracuse, E.M., Abers, G.A., 2011. Subduction factory: 4.
- Depth-dependent flux of H₂O from subducting slabs worldwide. J. Geophys. Res. 116,
- 704 B01401.
- Wallace, M.E., Green, D.H., 1988. An experimental determination of primary carbonatite
- magma composition. Nature 335, 343–346.
- Wallace, P.J., 2005. Volatiles in subduction zone magmas: Concentrations and fluxes based on
- melt inclusion and volcanic gas data. J. Volcanol. Geotherm. Res. 140, 217–240.
- Wyllie, P.J., 1978. Mantle Fluid Compositions Buffered in Peridotite-CO2-H2O by Carbonates,
- Amphibole, and Phlogopite. J. Petrol. 86, 687–713.

Zimmer, M.M., Plank, T., Hauri, E.H., Yogodzinski, G.M., Stelling, P., Larsen, J., Singer, B.,
 Jicha, B., Mandeville, C., Nye, C.J., 2010. The role of water in generating the calc-alkaline
 trend: New volatile data for aleutian magmas and a new tholeiitic index. J. Petrol. 51, 2411–
 2444.

715

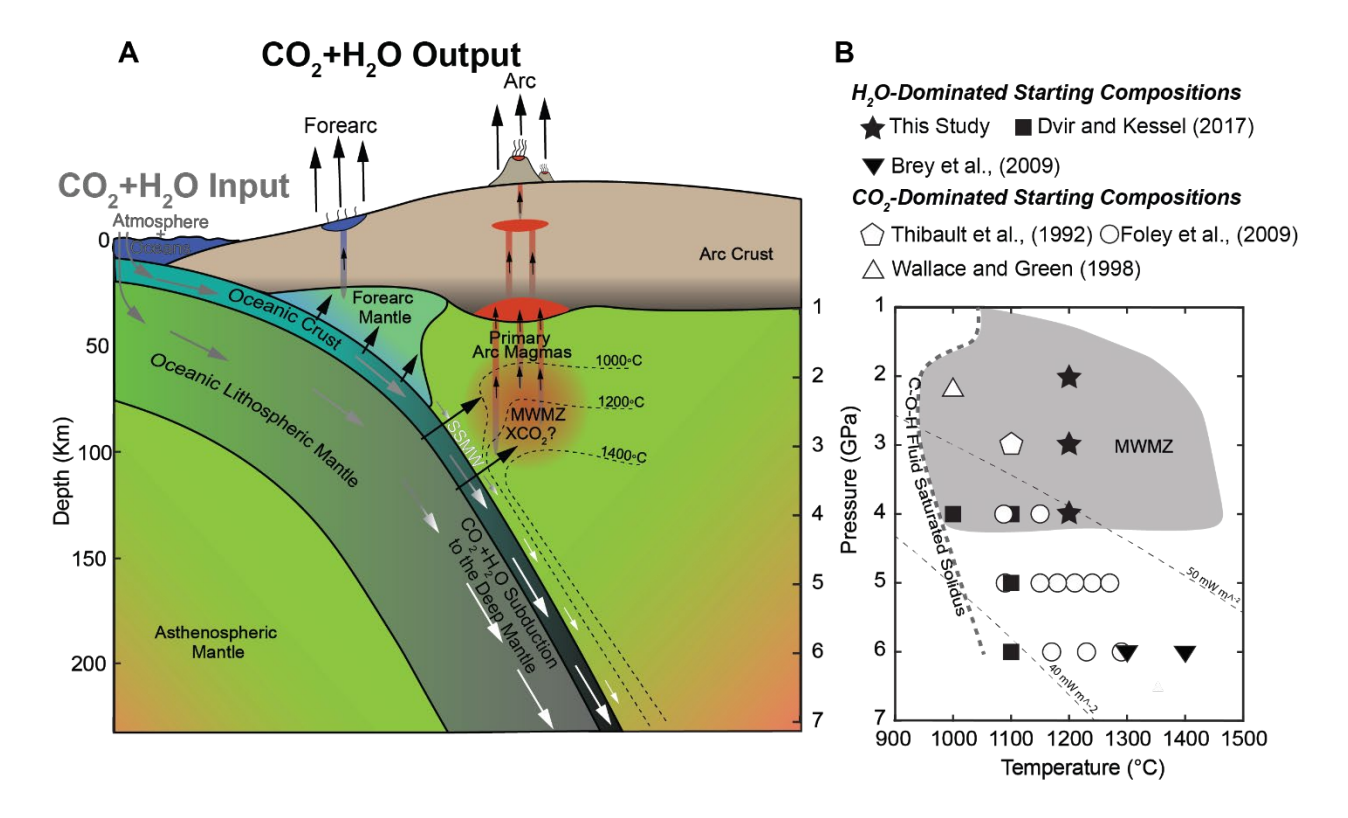


Fig. 1. (A) A schematic illustration of CO₂ and H₂O cycling in subduction zones. Grey arrows represent mineral bound CO2 and H2O fluxes into the mantle via subduction while black arrows represent CO₂ and H₂O fluxes from the slab to the forearc and mantle wedge melting zone (MWMZ). Any imbalance between these two fluxes equals the flux of CO₂ and H₂O to the deep mantle either carried by the slab (large white arrows) or by the adjacent sub-solidus mantle wedge (SSMW) dragged down by the slab (small white arrows). XCO₂ (CO₂/ (CO₂+ H₂O) in mol units) of fluids generating primary arc magmas in the MWMZ remains a key unknown parameter in the deep hydrogen and carbon cycles. Mantle wedge isotherms are from Syracuse et al. (2010) Alaska Peninsula – W1300 model. (B) Pressure and temperature conditions of the experiments in this study (black stars) compared to previous peridotite + H₂O + CO₂ experiments where melt compositions are well reported. H₂O dominated starting compositions (solid black symbols) are defined as those with $XCO_2 < 0.5$, while CO_2 dominated starting compositions (white symbols) are those with XCO₂ > 0.5. C-O-H fluid saturated solidus is from Falloon and Green (1990) from 1-3 GPa and Dvir and Kessel (2017) at 4-6 GPa. Grey region is the global range of mantle wedge P-T conditions from Syracuse et al. (2010), which lie above the C-O-H fluid saturated solidus, defining the *P-T* space of the MWMZ. Dotted lines are continental geotherms from Lee et al. (2011). Note that most previous studies are conducted in CO₂ dominated system at continental lithospheric mantel P-T conditions.

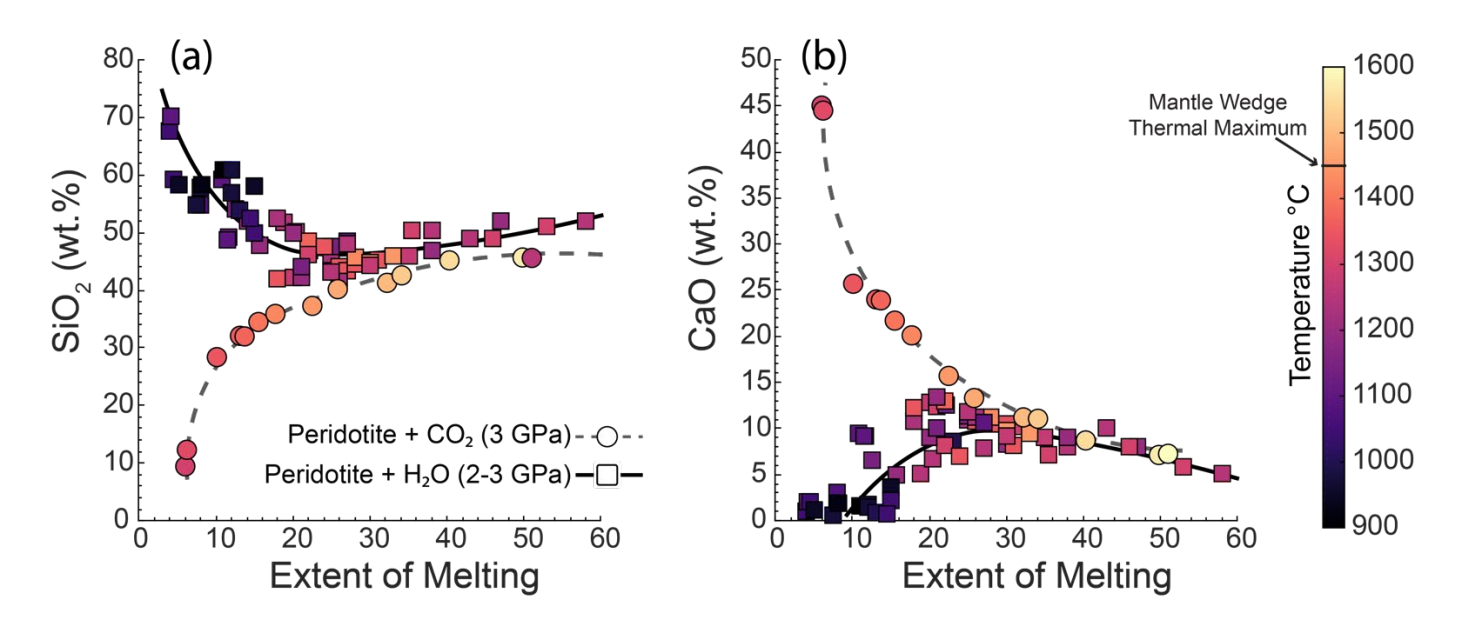


Fig. 2. SiO₂ (a) and CaO (b) contents of experimental partial melts from peridotite + CO₂ and peridotite + H₂O systems at 2-3 GPa plotted as a function of the extent of melting. All melts are plotted on a volatile free basis. Peridotite + CO₂ data are from Dasgupta et al. (2007) and peridotite + H₂O data are from Pirard and Hermann (2015), Mitchell and Grove (2015), Mallik et al. (2015, 2016), Grove and Till (2019), and Lara and Dasgupta (2020). Maximum mantle wedge temperature ~1450 °C is from Syracuse et al. (2010). Note the diverging behaviour of partial melt compositions in hydrous versus carbonated systems as the solidus is aproached.

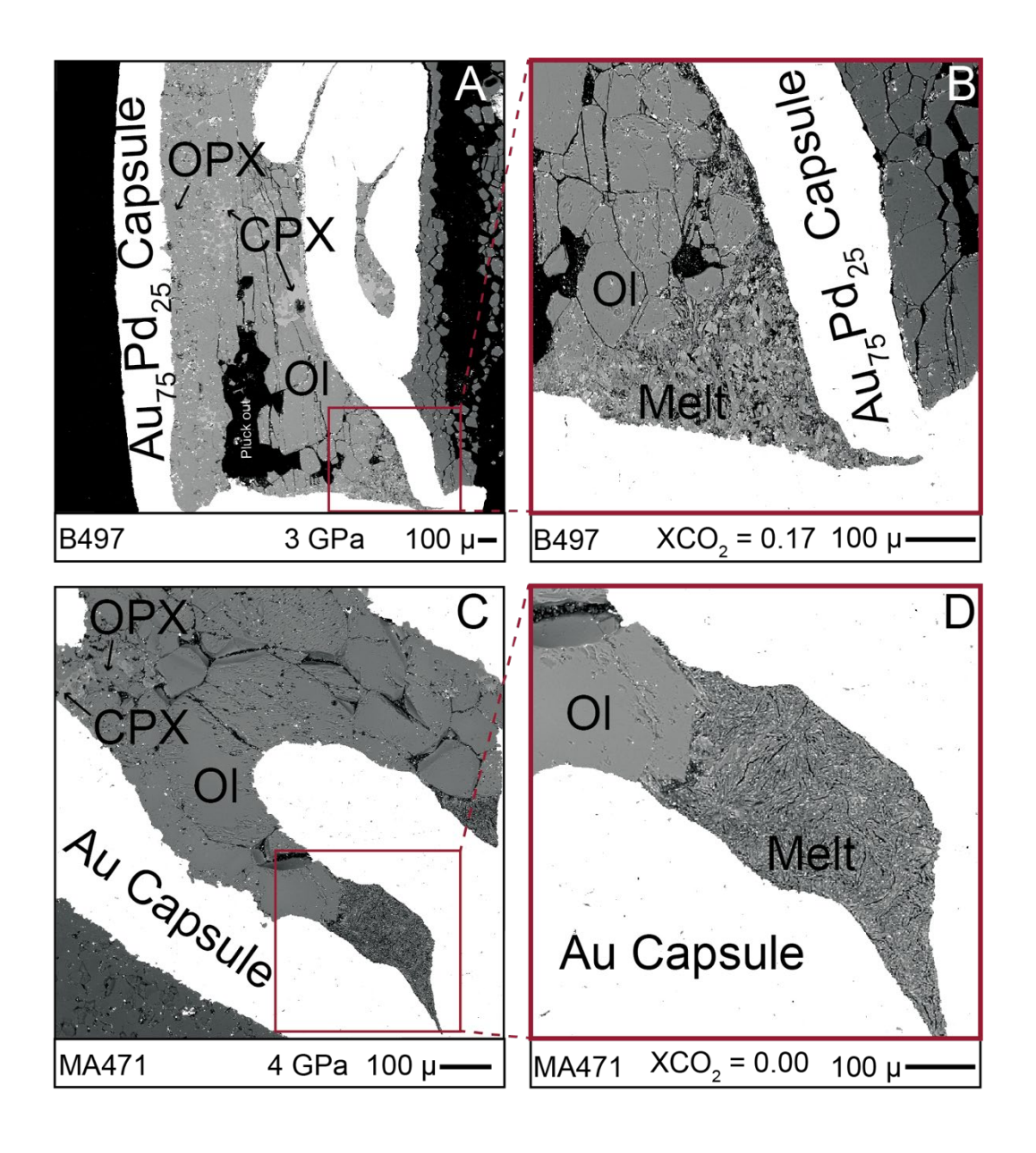


Fig. 3. BSE images of typical experiments on peridotite + H₂O ± CO₂ systems. (A) Full capsule BSE image of experiment B497 run at 3 GPa, 1200 °C using starting composition DP.17. The phase assemblage in this image (melt + olivine + opx + cpx) is characteristic of most experiments in this study. (B) Magnified image of H₂O-CO₂-bearing melt corresponding to red square in (A). Note that the quenched melt is an aggregate of exsolved metastable quench phases. (C) Full capsule BSE image of MA471 performed at 4 GPa, 1200 °C using the CO₂-free starting composition DP.00. Phase assemblage also consists of melt + olivine + opx + cpx. (D) Magnified image of H₂O-bearing melt corresponding to red square in (C). Similar to the H₂O-CO₂-bearing experiments, H₂O bearing melts are aggregates of exsolved metastable quench phases. In both peridotite + H₂O and peridotite + H₂O + CO₂ systems, olivines are concentrated towards and pyroxenes away from melt pools.

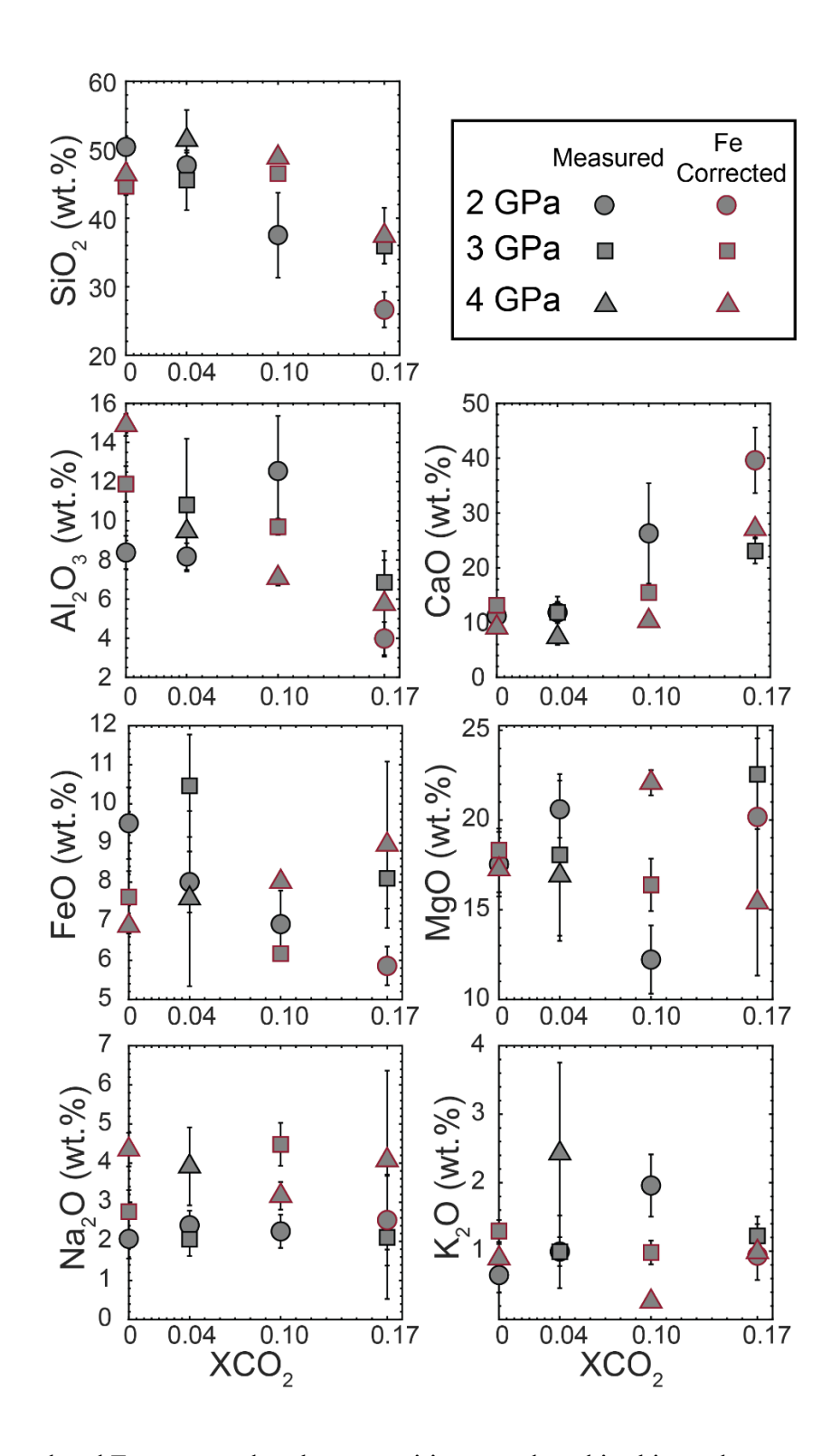


Fig. 4. Measured and Fe-corrected melt compositions produced in this study on a volatile-free basis plotted as a function of XCO_2 [= molar $CO_2/(CO_2+H_2O)$] of the starting compositions. $\pm 1\sigma$ error bars are based on replicate electron microprobe analyses. All melts were generated at a constant temperature of 1200 °C. Note that even at constant *P-T*; SiO₂, CaO, and Al₂O₃ partial melt compositions shift significantly as XCO_2 of bulk composition changes.

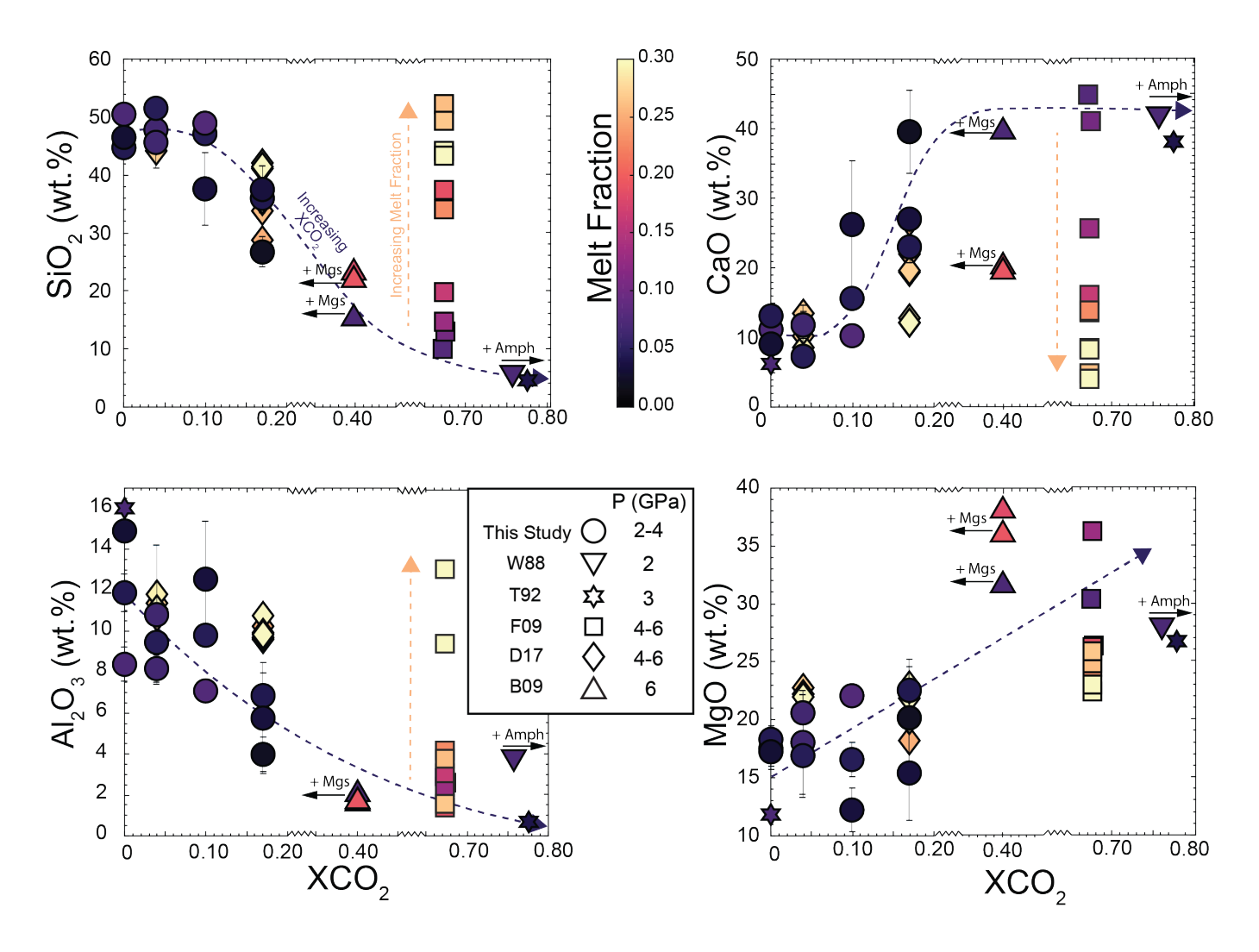


Fig. 5. Major element composition of experimental melts on a volatile free basis from this study and previous peridotite + H₂O + CO₂ studies as a function of melt fraction (color bar) and the nominal XCO₂ of the bulk composition. Previous studies – W88: Wallace and Green (1998); T92: Thibault et al. (1992); F09: Foley et al. (2009); D17: Dvir and Kessel (2017); B09: Brey et al. (2009). Purple curves show compositional trends of low degree melts as bulk XCO₂ increases, while the tan lines show compositional trends as melt fraction increases at a given bulk XCO₂. All curves and lines are nonquantitative and intended to guide the reader's eye. Black arrows show the effective XCO₂ of fluid available to dissolve in silicate melts in Brey et al. (2009) and Wallace and Green (1998), given magnesite (Mgs) and amphibole (Amph) were respectively present in these experiments. The breaks on the x axis cover XCO₂ ranges where experimental data is lacking. Vertical error bars on data from this study are ±1σ uncertainties based on replicate microprobe analyses, as given in Table 3.

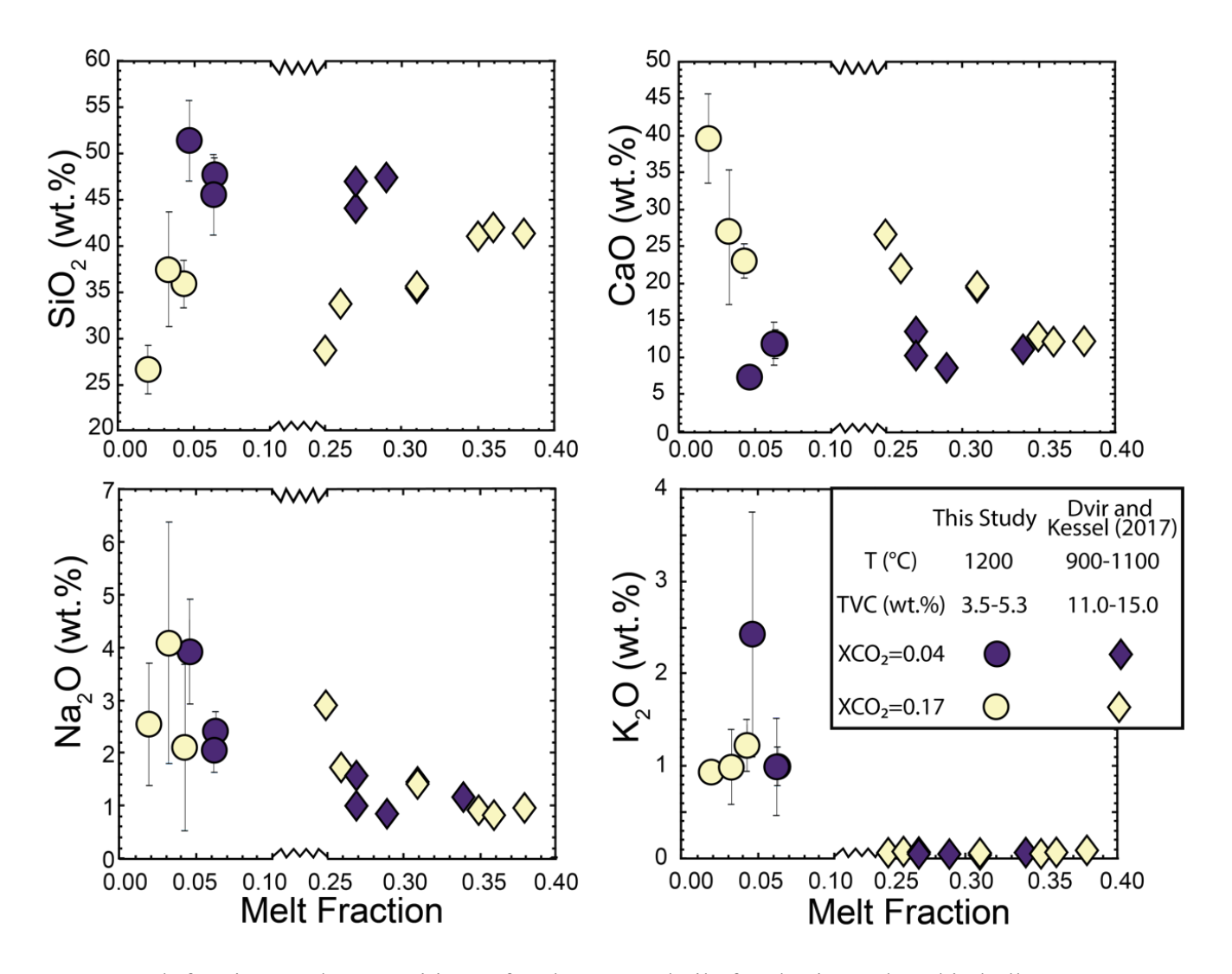


Fig. 6. Melt fractions and compositions of melts on a volatile free basis produced in bulk compositions with $XCO_2 = 0.04$ and 0.17 from this study and Dvir and Kessel (2017). TVC is the total volatile content ($H_2O + CO_2$) in wt.% of starting compositions. Vertical error bars for data generated in this study are $\pm 1\sigma$ uncertainties based on replicate microprobe analyses, as given in Table 3. Breaks in the x axis cover melt fractions not present in either study. Note that despite being run 100-300 °C cooler than the present study, melt fractions produced in the experiments of Dvir and Kessel (2017) are significantly higher than ours, reflecting the effect of TVC on the extent of melting. See discussion section 4.1.2 for details

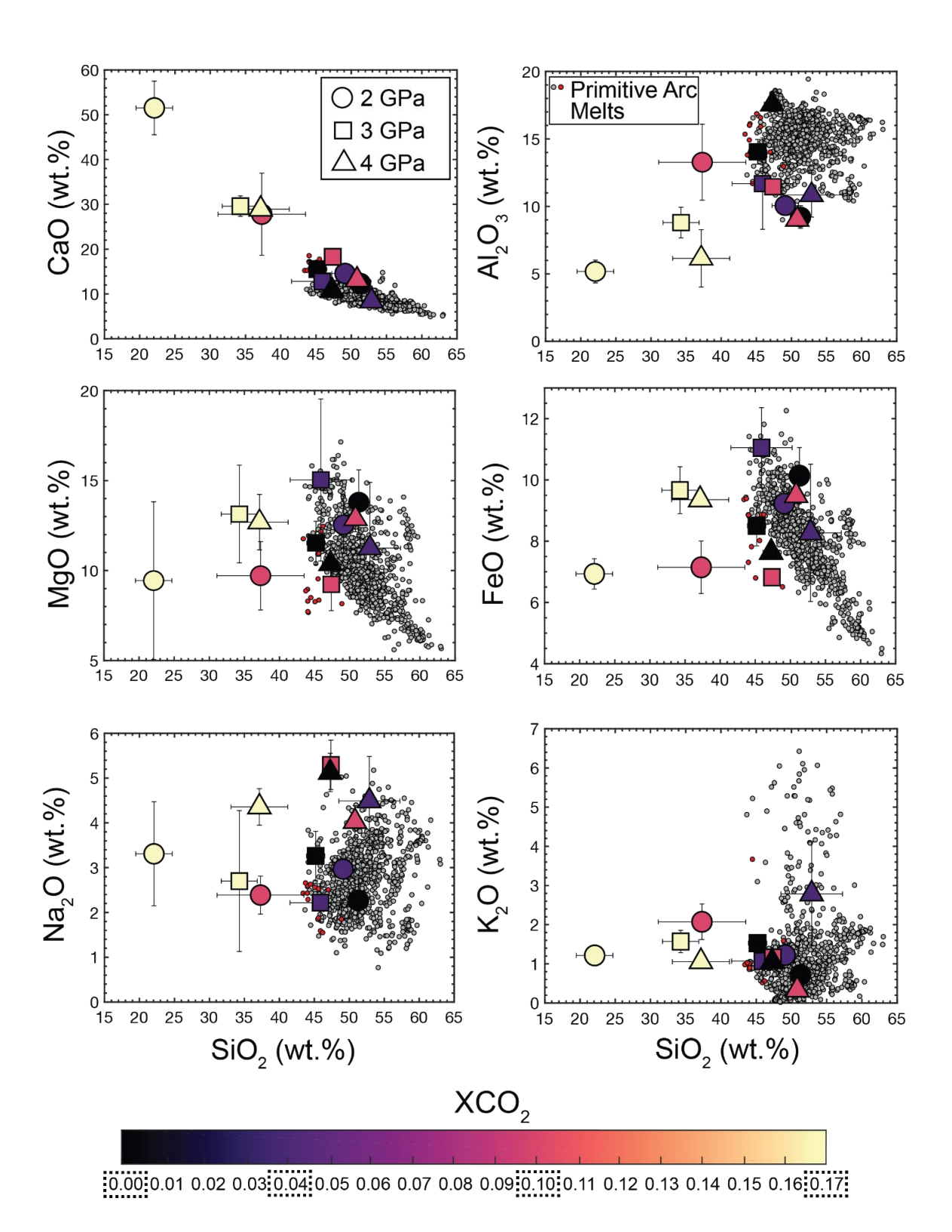


Fig. 7. Composition of olivine fractionation corrected experimental partial melts from this study compared to primitive arc lavas (Schmidt and Jagoutz, 2017: small grey circles and Schiano et al., 2000: small red circles). All melt compositions are reported on a volatile free basis. The corrected melt compositions are grouped according to the color bar, which represents the XCO_2 of the bulk compositions the melts were generated from. Black dashed boxes in the color bar represent the XCO_2 of our starting compositions. Note that melts produced in the bulk compositions with $XCO_2 = 0.17$ lie far from all primitive arc melts considered, suggesting that mantle wedge fluids have $XCO_2 < 0.17$. Error bars are $\pm 1\sigma$ uncertainties of the experimental melt compositions based on replicate microprobe analyses. See supplementary materials for fractionation correction details.

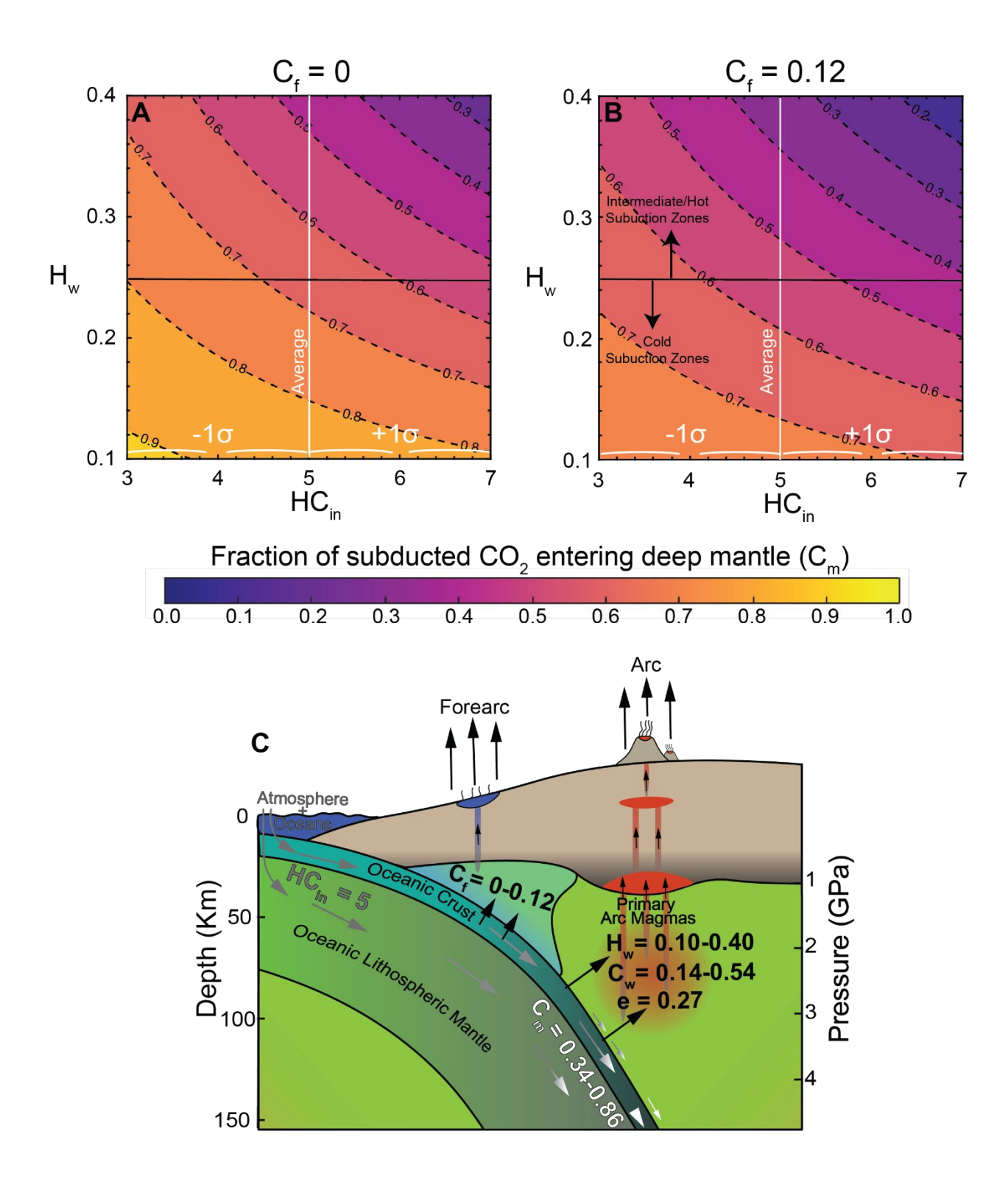


Fig. 8. The fraction of subducted CO_2 entering the deep mantle (C_m ; color coded field and contoured lines) as a function of the fraction of mineral bound H_2O , which is released to the mantle wedge (H_w), and the mineral bound H_2O/CO_2 ratio of incoming slabs (HC_{in}) for negligible C_f (A) or $C_f = 0.12$ (B). White vertical lines in each panel are the average HC_{in} with

 $\pm 1\sigma$ error determined by Monte Carlo simulations using H₂O and CO₂ flux estimates in Table 2. Black horizontal line discriminates between mantle wedge H₂O fluxes predicted for hot vs. cold subduction zones after Schmidt and Poli (1998). (C) Cartoon representing the quantity and location of each flux represented in equations 9 and 11 by setting HC_{in} = 5 and using our experimentally determined value e = 0.27.

Table 1 Experimental partial melt compositions

Run no	B500	B492	B494	B498	B499	B491	B495	B497	MA271	MA268	MA269	MA270
P (Gpa)	2	2	2	2	3	3	3	3	4	4	4	4
T (°C)	1200	1200	1200	1200	1200	1200	1200	1200	1200	1200	1200	1200
XCO_2	0	0.04	0.10	0.17	0	0.04	0.10	0.17	0.00	0.04	0.10	0.17
Method	Measured	Measured	Measured	Fe Corr ^B	Fe Corr	Measured	Fe Corr	Measured	Fe Corr	Measured	Fe Corr	Fe Corr
n ^A	18	20	21	25	12	11	23	10	15	8	30	6
Melt %	7.1 (3)	6.4 (5)	3.3 (2)	2.0 (2)	4.3 (1)	6.3 (6)	4.6 (7)	4.3 (2)	2.8 (3)	5 (1)	7.5 (2)	3.3 (2)
SiO_2	50 (1)	48 (2)	37 (6)	27 (3)	45 (1)	46 (4)	47 (1)	36 (3)	46 (1)	51 (4)	48.9 (8)	37 (4)
Al_2O_3	8.3 (8)	8.2 (7)	12 (3)	3.9 (8)	11.8 (9)	11 (3)	9.7 (4)	7 (1)	14.9 (6)	9 (2)	7.1 (4)	6 (3)
FeO*	9.5 (9)	8.0 (8)	6.9 (8)	5.9 (5)	7.6 (7)	10 (1)	6.2 (1)	8.1 (8)	6.9 (2)	8 (2)	8.0 (1)	9 (2)
MnO	0.25 (6)	0.25 (6)	0.3 (1)	0.2 (1)	0.34 (7)	0.23 (7)	0.32 (5)	0.19 (5)	0.20 (3)	0.9 (1)	0.24 (4)	0.3 (2)
MgO	17 (2)	20 (2)	12 (2)	20 (2)	18 (1)	18 (4)	16 (1)	22 (3)	17 (1)	17 (4)	22.1 (7)	15 (4)
CaO	11 (2)	12 (2)	26 (9)	40 (1)	13 (1)	12 (6)	15 (1)	23 (2)	9 (1)	7 (1)	10.3 (4)	27 (2)
Na₂O	2.0 (5)	2.4 (4)	2.3 (4)	3 (1)	2.8 (5)	2.0 (4)	4.5 (5)	2 (1)	4.3 (4)	4 (1)	3.2 (4)	4 (3)
K_2O	0.6 (3)	1.0 (2)	1.9 (5)	0.9 (5)	1.3 (2)	1.0 (5)	1.0 (2)	1.2 (3)	0.9 (2)	2 (1)	0.26 (8)	1.0 (4)
Mg# ^C	0.76	0.82	0.76	0.86	0.81	0.75	0.83	0.83	0.82	0.80	0.83	0.75
K_D^D	0.27	0.40	0.24	0.43	0.39	0.24	0.43	0.41	0.41	0.30	0.40	0.33
DPT^E	33 (8)	27 (9)	26 (4)	28 (5)	23 (8)	19 (7)	19 (3)	28 (4)	19 (3)	36 (8)	20 (2)	43 (4)

Melt compositions reported on a volatile-free basis in wt.%. $\pm 1\sigma$ error based on replicate electron microprobe analyses are reported in parentheses. \pm 1 σ error are reported as least digits cited. For example, 46 (4) should be read as 46 \pm 1 wt.% and 14.9 (6) as 14.9 \pm 0.6 wt.%.

^A Number of analyses.

^B Fe corrected melt composition based on Fe loss to Au₇₅Pd₂₅ and Au capsules. ^C Mg# = molar MgO/ (MgO + FeO*)

^D Fe – Mg
$$Kd_{melt}^{ol} = \frac{X_{FeO}^{ol}}{X_{FeO}^{Melt}} \times \frac{X_{MgO}^{Melt}}{X_{MgO}^{ol}}$$

Table 2.

Volatile flux estimates in subduction zones from previous studies and estimation of variables in equation 11.

	H ₂ O _{in}	CO _{2in}	CO _{2f}	H_2O_w	HCin	${ m C_f}^{ m C}$	$H_{ m w}^{ m D}$
<u>Variable</u>	$(10^{14} \text{g}/7)$	(10^{14}g/y)	(10^{14}g/y)	(10^{14}g/y)	(nd ^A)	(nd)	(nd)
Jarrard (2003)	7.38*	1.52*			4.9		
Dasgupta and Hirschmann (2010)		2.2 - 4.2					
Dasgupta (2013)		2.0-3.2					
Kelemen and Manning (2015)		1.5 - 2.4	0.004 - 0.07			.00303	
Plank and Manning (2019)		2.5 - 3.5					
Van Keken et al. (2011)	7.0 - 10.0			1.0 - 1.4			0.14
Hacker (2008)	13.3						
Peacock (1990)	8.7*						0.10
Bebout (1995)	9.3 - 19.4*						
Rupke et al (2004)	9.0 - 18.0						
Barry et al. (2019) ^E		0.04	0.0005 - 0.005			0.001 - 0.12	
Schmidt and Poli (1998)							0.18 - 0.37
Ito et al. (1981)							0.1
Estimate ^F					5 ± 2	0 - 0.12	0.1 - 0.4

^A Non-dimensional number

^E Difference between 100% and measured probe totals for melts.

^B Flux of mineral-bound H₂O divided by flux of CO₂ entering subduction zones.

^C Flux of CO₂ entering fore-arc mantle divided by flux of CO₂ entering subduction zones.

^D Flux of H₂O entering mantle wedge divided by flux of H₂O entering subduction zones.

^E Not a global estimate. Only an estimate based on the Costa Rican subduction zone. F Our estimates for the variables in equation 11 using flux estimates from existing literature * Does not include oceanic lithospheric mantle in estimate.